ELSEVIER

Volume 184, Issue 8, August 2011

JOURNAL OF SOLID STATE CHEMISTRY

www.elsevier.com/locate/jssc

CONTENTS

Abstracted/indexed in BioEngineering Abstracts, Chemical Abstracts, Coal Abstracts, Current Contents/Physics, Chemical, & Earth Sciences, Engineering Index, Research Alert, SCISEARCH, Science Abstracts, and Science Citation Index. Also covered in the abstract and citation database SCOPUS®. Full text available on ScienceDirect®.

Regular Articles

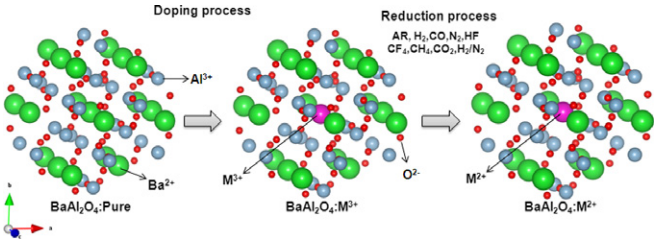

The doping and subsequent reduction of a rare earth ion into the barium aluminate lattice.

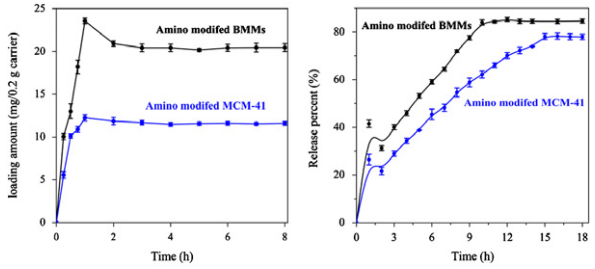

Loading (A) and release profiles (B) of aspirin in N-BMMs and N-MCM-41 indicated that BMMs have more drug loading capacity and faster release rate than that MCM-41.

Regular Articles—Continued

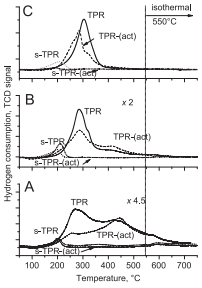

TPR, TPR-(act), s-TPR and s-TPR-(act) profiles of (*1.36*)Cu/SAPO-5 (A), (*4.55*)Cu/SAPO-5 (B) and (*9.19*)Cu/SAPO-5 (C) samples. The intensities of TCD signals in (A) and (B) are multiplied by 4.5 and 2, respectively.

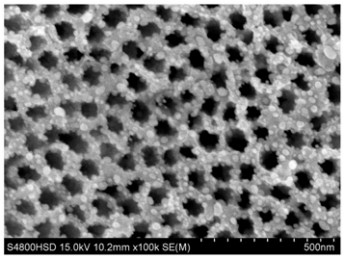

Ag–$SrTiO_3$ nanotube arrays were successfully prepared. The photocatalytic activity was evaluated by degradation of methyl orange under ultraviolet irradiation.

Continued

Photoluminescence and energy transfer in Tb^{3+}/Mn^{2+} co-doped $ZnAl_2O_4$ glass ceramics
Gandham Lakshminarayana and Lothar Wondraczek
page 1931

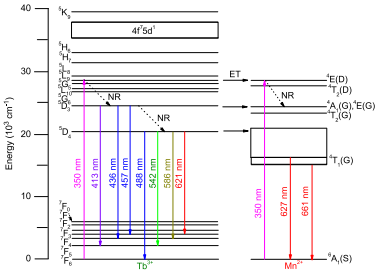

In the prepared Tb^{3+}/Mn^{2+} codoped glass ceramics containing gahnite ($ZnAl_2O_4$) nanocrystals, the luminescence color is changed from green light to yellowish-red light with an increase in Mn^{2+} concentration due to enhanced energy transfer from Tb^{3+} to Mn^{2+} ions. This tunability should have potential applications in solid state lighting to produce white light, which can be obtained by appropriately optimizing the ratio of Tb^{3+}/Mn^{2+} ions under UV(350 nm) excitation.

Preparation and physical properties of antiperovskite-type compounds $CdNCo_{3-z}Ni_z$ ($0 \le z \le 3$)
Bing He, Cheng Dong, Lihong Yang, Linhui Ge and Hong Chen
page 1939

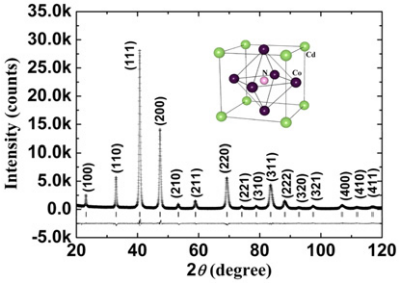

$CdNCo_3$ is a new ternary nitride with antiperovskite structure, and it can form a complete solid solution series with $CdNNi_3$.

Structural and optical properties of Ga_2O_3:In films deposited on MgO (1 0 0) substrates by MOCVD
Lingyi Kong, Jin Ma, Caina Luan and Zhen Zhu
page 1946

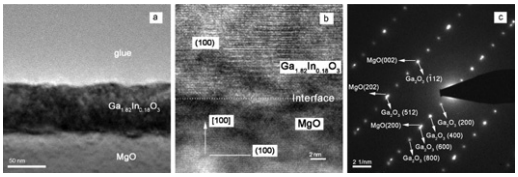

Low magnification XTEM (a), HRTEM (b) and SAED (c) micrographs of the interface area between $Ga_{1.82}In_{0.18}O_3$ film and MgO substrate have showed the $Ga_{1.82}In_{0.18}O_3$ is an epitaxial film.

High-temperature electron–hole transport in $PrBaCo_2O_{5+\delta}$
A.Yu. Suntsov, I.A. Leonidov, M.V. Patrakeev and V.L. Kozhevnikov
page 1951

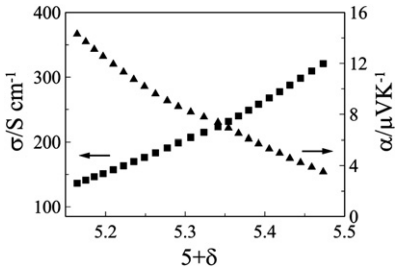

Electrical properties in $PrBaCo_2O5+\delta$ depending on oxygen content at 800 °C.

One-pot synthesis, optical property and self-assembly of monodisperse silver nanospheres
Aiwei Tang, Shengchun Qu, Yanbing Hou, Feng Teng, Yongsheng Wang and Zhanguo Wang
page 1956

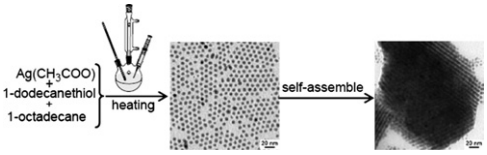

Different sized and monodisperse silver nanospheres were prepared using a one-pot approach with no pre-synthesis of organometallic precursors, and the silver nanospheres can self-assemble into highly ordered superlattices.

Di-, tri-, tetranuclear clusters and polymeric cadmium compounds: Syntheses, structures and fluorescent properties with various linking fashions and high stability of orotates under the condition of strong bases
Xing Li, Yue Bing, Mei-Qin Zha, Dong-Jie Wang, Lei Han and Rong Cao
page 1963

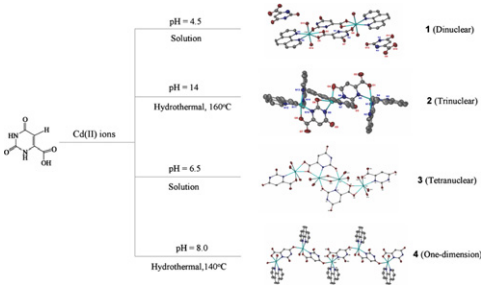

Assembly of orotic acid and Cd(II) salts result in four new compounds under different reaction conditions, the compounds possess strong photoluminescence emissions and high thermal stability.

Synthesis and electronic properties of *Ln*RhAsO and *Ln*IrAsO compositions
Sean Muir, A.W. Sleight and M.A. Subramanian
page 1972

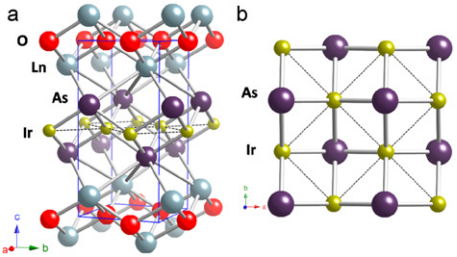

*Ln*IrAsO (*Ln* = La, Ce, Nd) and *Ln*RhAsO (*Ln* = Ce, Rh) have been synthesized. These new transition metal oxypnictide compositions are isostructural to LaFeAsO. The 5*d* Ir compositions demonstrate a shorter metal-metal interaction than the 4*d* Rh compositions.

Preparation and visible light photocatalytic activity of Bi_2O_3/Bi_2WO_6 heterojunction photocatalysts
Ming-Sheng Gui, Wei-De Zhang, Qing-Xi Su and Cai-Hong Chen
page 1977

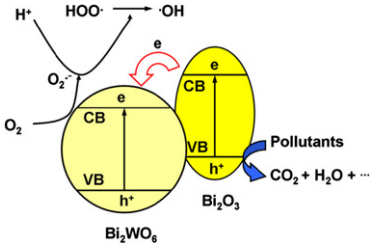

The Bi_2O_3/Bi_2WO_6 heterojunction catalysts were constructured with improved photocatalytic activity, which can be ascribed to their improved light absorption property and the reduced recombination rate between photoexcited electrons and holes.

Investigation of the silicon concentration effect on Si-doped anatase TiO_2 by first-principles calculation
Weimei Shi, Qifeng Chen, Yao Xu, Dong Wu and Chun-fang Huo
page 1983

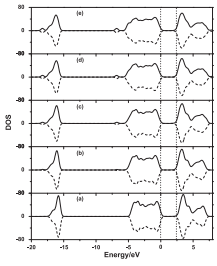

The total density of states (TDOS) of $Ti_{1-x}Si_xO_2$ with (a) $x = 0$, (b) $x = 0.03125$, (c) $x = 0.0625$, (d) $x = 0.09375$ and (e) $x = 0.125$.

Phase-controlled solvothermal synthesis and characterization of nickel sulfides with good single crystalline nature
Shuguang Chen, Kai Zeng, Haibin Li and Fujin Li
page 1989

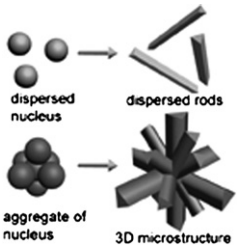

Rhombohedral NiS dispersed rods and 3D flower-like microstructures are evolved from dispersed nucleus and aggregate of nucleus, respectively, and the cross-sections of such rods are in equilateral triangle-like shape.

Pressure-induced development of bonding in NiAs type compounds and polymorphism of NiP
Przemyslaw Dera, John D. Lazarz and Barbara Lavina
page 1997

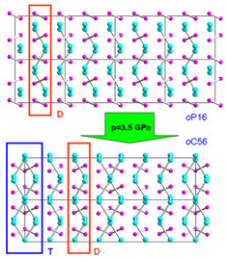

A reversible, pressure-induced phase transition has been found in nickel monophosphide NiP at 3.5 GPa by means of in situ single-crystal X-ray diffraction. The high-pressure phase is a commensurately modulated superstructure of the NiAs aristotype involving gradual conversion from the net of isolated P_2 dimers found in the ambient NiP, towards zig-zag polymeric P_∞ chains found in MnP.

Crystal structure of $LiLnW_2O_8$ (*Ln* = lanthanides and Y): An X-ray powder diffraction study
J.M. Postema, W.T. Fu and D.J.W. IJdo
page 2004

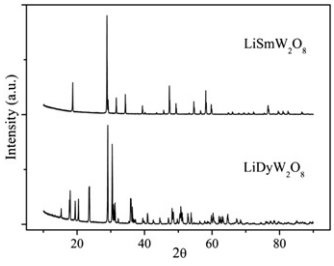

Part of the X-ray diffraction patterns of $LiSmW_2O_8$ and $LiDyW_2O_8$ representing two structure types in $LiLnW_2O_8$: the scheelite with *Ln* = La–Gd and wolframite with *Ln* = Dy–Lu and Y. In $LiTbW_2O_8$ both the scheelite and the wolframite structures occur at high and low temperatures, respectively.

Continued

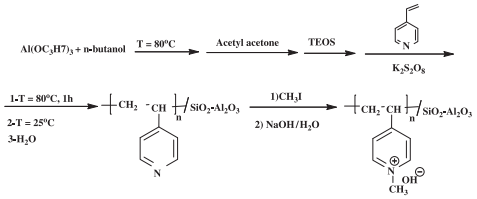

In this paper, we report the synthesis of poly 4-methyl vinyl pyridinium hydroxide–SiO_2–Al_2O_3. The novelty of this procedure is at easy preparation together with using inexpensive materials.

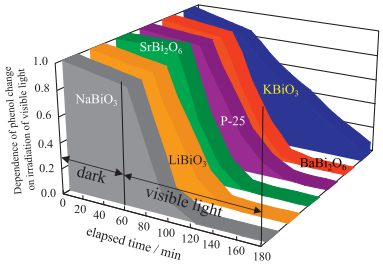

Nine pentavalent bismuthates were synthesized and were examined for their photocatalytic activities by decomposition of phenol under visible light irradiation. $NaBiO_3$, $LiBiO_3$, $SrBi_2O_6$ and $BaBi_2O_6$ indicated faster decomposition rate than that of anatase (P25) under UV–vis light irradiation.

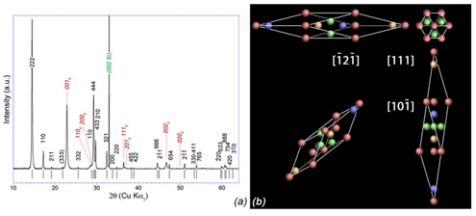

(a) θ/2θ X-ray pattern of the tantalum oxide layer prepared by i-MOCVD, cooled down at 5 °C min^{-1} after a thermal treatment at 850 °C under N_2 for 1 h. (b) Rhombohedral cell of the Ta_2O_5 trigonal structure of *R*3 space-group decorated with its 10 Ta sites.

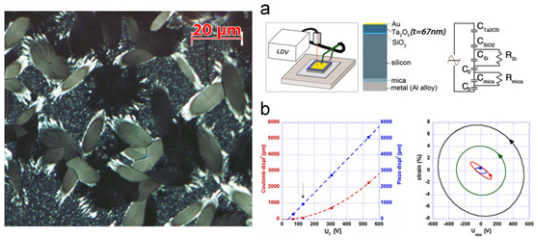

Image of cross-polarized optical microscopy showing grains of trigonal structure embedded in the monoclinic phase (on the left); (a) mounting of the sample for Laser Doppler Vibrometry, sample constituted of several layers and its equivalent electrical circuit; (b) longitudinal displacements due to converse piezoelectric and Coulomb effects and corresponding piezoelectric strain–$U_{app.}$ hystereses.

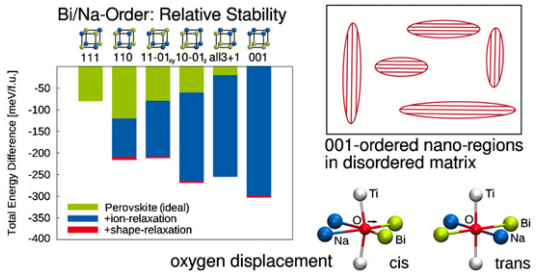

First-principles calculations give relative stabilities of different chemically ordered structures. The results suggest a new model for the local structure of $Na_{1/2}Bi_{1/2}TiO_3$ with 001-ordered nano-regions embedded in a chemically disordered matrix. Chemical order/disorder additionally induces displacive disorder within the oxygen sublattice.

Increasing the gelation temperature, the particle shapes changed from sphere-like particles at 65 °C to a particle chain at 75 °C, and then form rod-like particles at 85 °C.

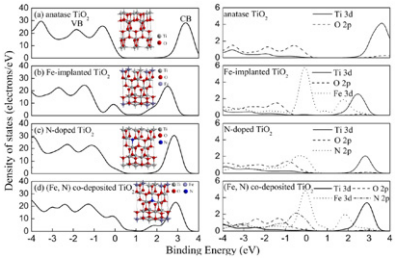

The electronic properties of (Fe, N) co-deposited TiO_2 films determined by theoretical calculations is graphically shown; Fe and N preferentially substitute the Ti and O site, to form impurity level.

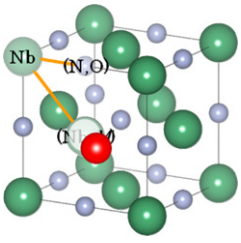

Doped silicon ions substituting Nb in $(Nb_{0.87}Si_{0.09}\square_{0.04})(N_{0.87}O_{0.13})$ introduced a large displacement at the 4*a* site mainly because of the accompanied vacancy. The silicon ions may also be slightly shifted from the regular octahedral 4*a* site (green) towards the interstitial tetrahedral site (red) statistically in the rock-salt type lattice.

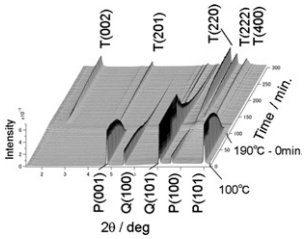

Time-resolved XRD data set was obtained at up to 190 °C under a saturated steam pressure. Tobermorite ($5CaO \cdot 6SiO_2 \cdot 5H_2O$) formation reaction was investigated in detail for several different starting materials.

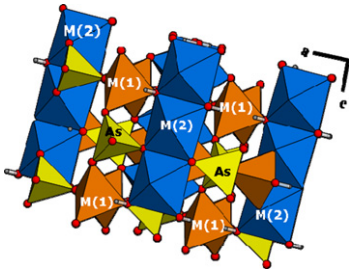

Schematic drawing of the $Co_{2-x}Cu_x(OH)AsO_4$ (x = 0 and 0.3) crystal structure view along the $[0\,1\,0]$ direction. Polyhedra are occupied by the M(II) ions (M = Co and Cu) and the AsO_4 groups are represented by tetrahedra. Open circles correspond to the oxygen atoms, and small circles show the hydrogen atoms.

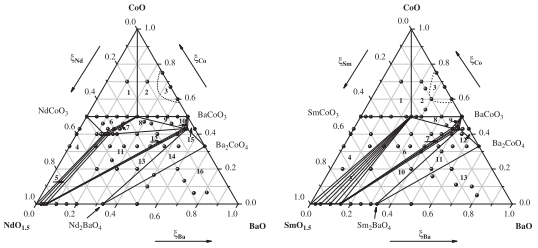

Projections of isobaric isothermal phase diagrams of the Nd–Ba–Co–O system and Sm–Ba–Co–O system.

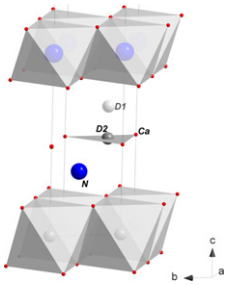

$Ca_2ND_{0.90}H_{0.10}$ forms a mixture of ordered and disordered phases when synthesised at 600 °C. The ordered phase disappears at high temperature upon release of structural deuterium/hydrogen, leaving a single, partially disordered phase.

Continued

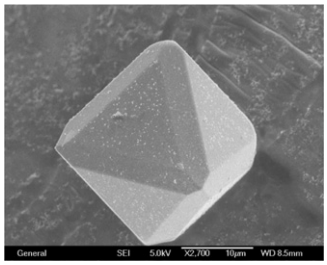

The Cu_2O crystals with truncated octahedral shape were one-step synthesized in high yield via high pressure flux method for the first time, which is green and environmentally friendly. The mechanisms of synthesis and crystal growth were discussed in this paper.

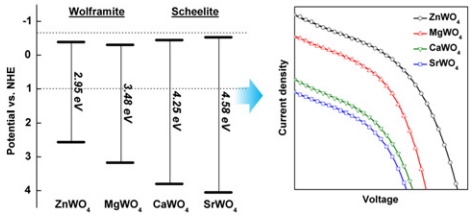

The electronic band structures of divalent metal tungstates are described from the combination of experimental results and theoretical calculations, and their electronic structure-dependent photovoltaic performances are also studied.

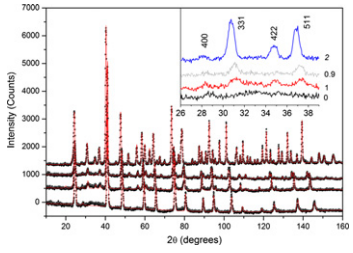

Neutron diffraction profiles for $Nd_{2-y}Ho_yZr_2O_7$ type oxides reveal details of the transformation from the ordered pyrochlore structure ($y = 0$) to the disordered fluorite structure ($y = 2$).

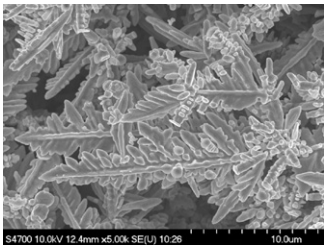

Uniform dendritic Cu are grown through controlling $V_{glycerol/water}$ in range of 0.6–1.2 and the concentration of H_3PO_3 in range of 0.06–0.3 M. The rhombic cluster Cu are obtained by decreasing the amount of glycerol.

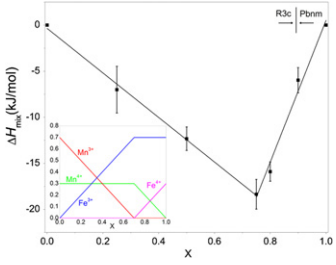

Enthalpy of mixing (ΔH_{mix}) of $La_{0.7}Sr_{0.3}Mn_{1-x}Fe_xO_{3-\gamma}$ solid solution at room temperature as a function of Fe/(Fe + Mn) ratio, x. Linear fits for the two regions at low and high x are shown as solid lines. The inset shows the content of Mn^{3+}, Mn^{4+}, Fe^{3+} and Fe^{4+} as a function of x based on the work by Jonker [18]. The redox reactions between different valence states of Fe and Mn dominate the energetic behavior of the solid solution.

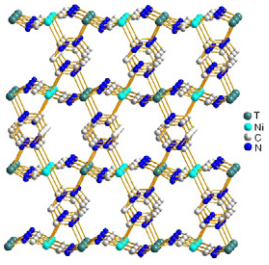

Rippled sheets structure for the pillared solids $T[Ni(CN)_4] \cdot 2pyz$. The pyrazine molecule is found forming T–pyz–Ni bridges between neighboring layers.

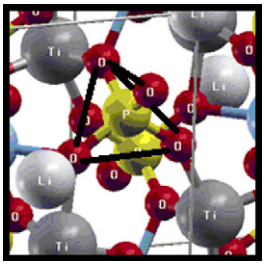

It is shown that P is tetrahedrally coordinated by four O ions.

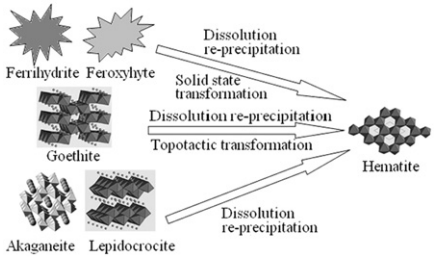

The transformation of various iron oxyhydroxides in the presence of trace Fe(II) was compared based on experimental results, thermodynamic stability, crystalline structure, and transformation mechanism.

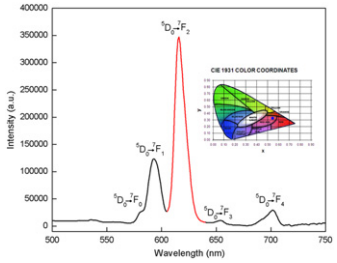

Luminescence spectrum of the PTBEu20 glass with CIE coordinates.

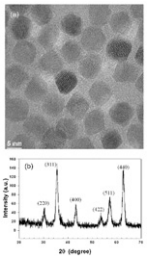

(a) HRTEM image of oleic acid capped MPs. The size of MPs ranges from 8 to 10 nm. (b) XRD pattern of γ-Fe_2O_3 MPs.

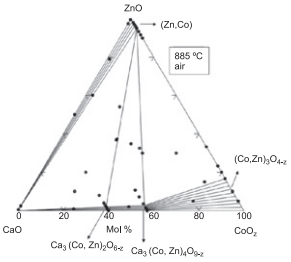

Phase diagram of the CaO–CoO_x–ZnO system at 885 °C in air, showing the limits of various solid solutions, and the tie-line relationships of various phases.

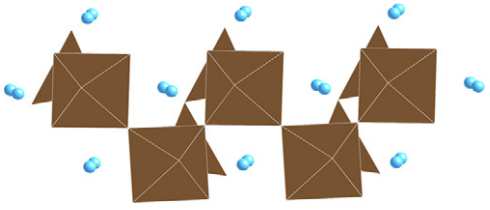

Preferential substitution by zinc for iron at the tetrahedral sites of brownmillerite dicalcium ferrite modifies the high temperature *Imma*(0 0 γ)s00 phase from incommensurate to commensurate.

Continued

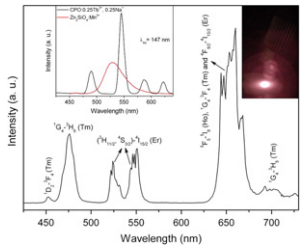

The CPO:0.25Tb^{3+}, 0.25Na^+ exhibits a comparable brightness to the commercial Zn_2SiO_4:Mn^{2+} upon 147 nm excitation. Good white light color is achieved in CPO:Yb^{3+}–Tm^{3+}–Er^{3+}–Ho^{3+} under 980 nm excitation.

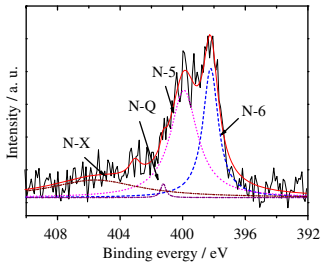

The N_{1s} spectra of nitrogen functionalized multi-walled carbon nanotubes are measured by X-ray photoelectron spectroscopy.

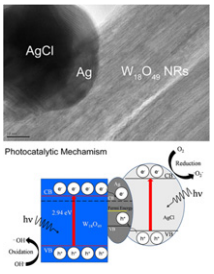

The Ag/AgCl nanoparticles adhered well to the $W_{18}O_{49}$ nanorod. The Ag could act as transfer center of the photoexcited carriers, prohibiting their recombinations in both $W_{18}O_{49}$ and AgCl.

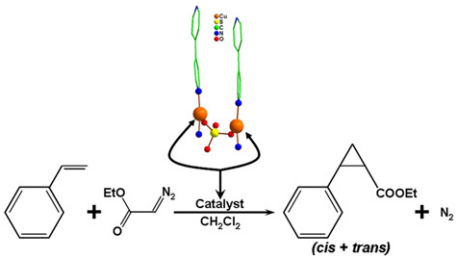

A new MOF structure built up of 4,4′-bipyridine, sulphate and Cu(I), is an active heterogeneous catalyst for cyclopropanation of styrene with ethyldiazoacetate.

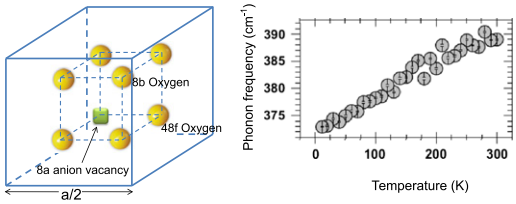

The phonon–phonon anharmonic interaction which is responsible for the temperature-dependent anomalous behavior of phonons, arise due to the inherent vacant sites in the pyrochlore structure.

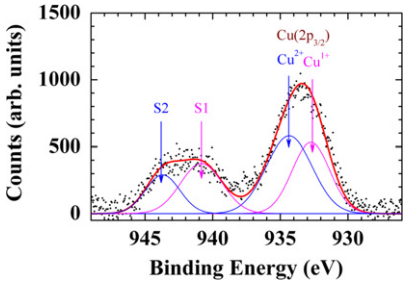

Cu_2O octahedra were found to have thin layer of CuO, due to oxidation of surface Cu^+ atoms by the surfactant O atoms.

Multifunctional properties of CoNi alloy embedded in the SiO_2 host: Role of interparticle interaction
S. Das, S. Majumdar and S. Giri
page 2215

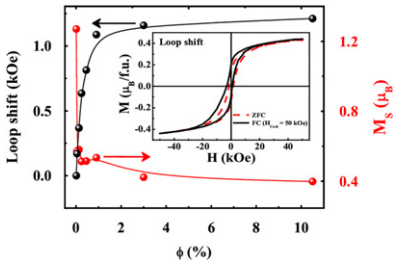

Plot of loop shift (left axis) and saturation magnetization (right axis) with volume fraction (ϕ). Inset: loop shift after field-cooling with 50 kOe field and no shift after zero-field-cooling.

The binary tin-rich lanthanum stannides La_2Sn_5 and La_3Sn_7—A structural and bond theoretical study
Ines Dürr, Michael Schwarz and Caroline Röhr
page 2220

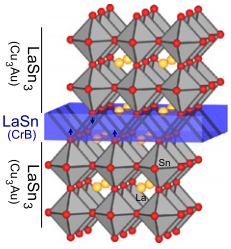

La_2Sn_5 and La_3Sn_7, stacking variants of $LaSn_3$ (Cu_3Au type, *closo* clusters) and LaSn (CrB type, zig-zag chains).

Structure and properties of a novel cobaltate $La_{0.30}CoO_2$
K. Knížek, J. Hejtmánek, M. Maryško, E. Šantavá, Z. Jirák, J. Buršík, K. Kirakci and P. Beran
page 2231

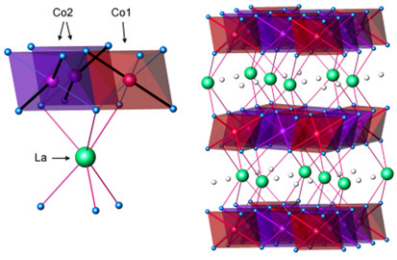

Optimized superstructure of $La_{0.3}CoO_2$ obtained by LDA calculation.

X-ray photoelectron (XPS) and Diffuse Reflectance Infra Fourier Transformation (DRIFT) study of $Ba_{0.5}Sr_{0.5}Co_xFe_{1-x}O_{3-\delta}$ (BSCF: $x = 0$–0.8) ceramics
Jae-Il Jung and Doreen D. Edwards
page 2238

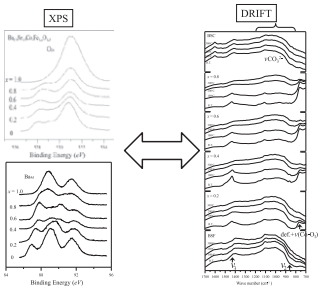

The bonding of CO_3^{2-} to the surface of BSCF perovskite and the bonding state between cations vs. oxygen have been suggested.

Enhanced visible-light absorption and dopant distribution of iodine-TiO_2 nanoparticles synthesized by a new facile two-step hydrothermal method
Xiaoting Hong, Zhiping Luo and James D. Batteas
page 2244

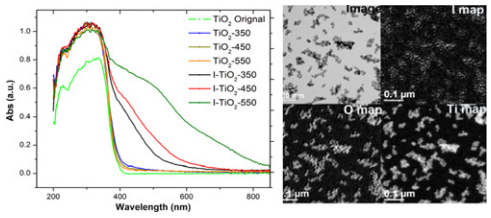

As-synthesized I-TiO_2 nanoparticles show significantly enhanced visible-light absorption, with the dopant iodine homogenously dispersed on each I-TiO_2 nanostructure based on EELS elemental mapping.

Insights into photoluminescence property and photocatalytic activity of cubic and rhombohedral $ZnIn_2S_4$
Shaohua Shen, Penghui Guo, Liang Zhao, Yuanchang Du and Liejin Guo
page 2250

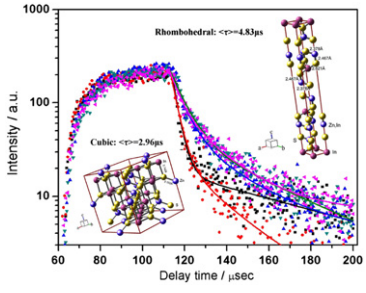

Rhombohedral $ZnIn_2S_4$ showed a superior photocatalytic activity for H_2 evolution than cubic $ZnIn_2S_4$, which was proved to be related with their different dynamics of photogenerated carriers.

Continued

Surfactant-assisted hydrothermal crystallization of nanostructured lithium metasilicate (Li_2SiO_3) hollow spheres: II—Textural analysis and CO_2–H_2O sorption evaluation

José Ortiz-Landeros, Carlos Gómez-Yáñez and Heriberto Pfeiffer

page 2257

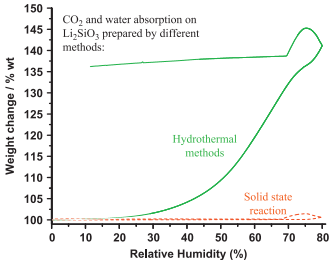

Li_2SiO_3 varied significantly its capacity of CO_2 absorption as a function of the microstructural properties and by the water presence.

Synchrotron and neutron powder diffraction study of phase transition in weberite-type Nd_3NbO_7 and La_3NbO_7

Lu Cai and Juan C. Nino

page 2263

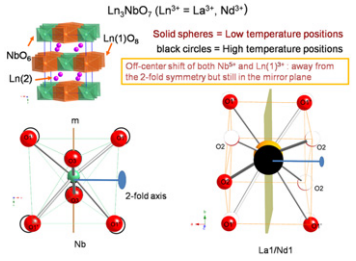

The phase transition of La_3NbO_7 and Nd_3NbO_7 upon cooling primarily involves the off-center shifting of Nb^{5+} ions inside the NbO_6 octahedra, combined with shifts of one third of the Ln^{3+} (Ln^{3+} = La^{3+} and Nd^{3+}) ions at the center of the LnO_8 polyhedra towards off-center positions. Above the phase transition temperature, Ln^{3+} and Nb^{5+} sit at a position with mirror symmetry and 2-fold axis. Below the phase transition temperature, Ln^{3+} and Nb^{5+} shift away from the 2-fold axis but still in the mirror plane.

A high temperature diffraction-resistance study of chalcopyrite, $CuFeS_2$

T.E. Engin, A.V. Powell and S. Hull

page 2272

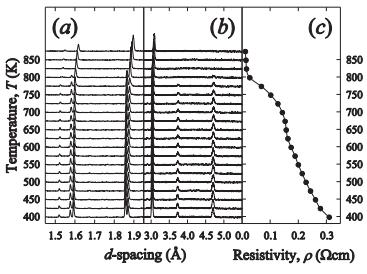

Structural, magnetic and electrical properties of $CuFeS_2$ to 873 K have been investigated using DC resistance measurements, performed in-situ during the collection of powder neutron diffraction data.

Synthesis and structural characterization of $Al_7C_3N_3$-homeotypic aluminum silicon oxycarbonitride, $(Al_{7-x}Si_x)(O_yC_zN_{6-y-z})$ (x∼1.2, y∼1.0 and z∼3.5)

Daisuke Urushihara, Motoaki Kaga, Toru Asaka, Hiromi Nakano and Koichiro Fukuda

page 2278

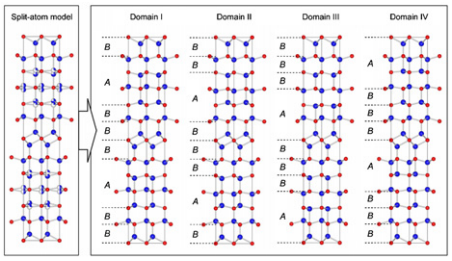

A new oxycarbonitride discovered in the Al–Si–O–C–N system, $(Al_{7-x}Si_x)(O_yC_zN_{6-y-z})$ (x∼1.2, y∼1.0 and z∼3.5). The crystal is composed of four types of domains (I, II, III and IV), and hence the structure is represented by a split-atom model. Individual crystal structures can be regarded as layered structures, which consist of *A*-type [(Al, Si)$_4$(O, C, N)$_4$] unit layers and *B*-type [(Al, Si)(O, C, N)$_2$] single layers.

Selective formation of VO_2(A) or VO_2(R) polymorph by controlling the hydrothermal pressure

Shidong Ji, Feng Zhang and Ping Jin

page 2285

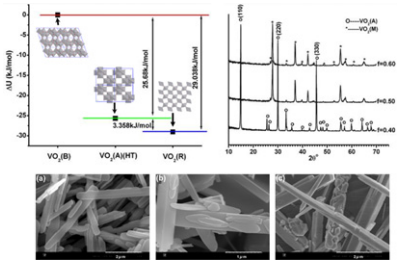

Selective formation of VO_2(A) or VO_2(R) could be achieved by controlling the system pressure through varying the filling ratio during hydrothermal treatment.

Crystal growth, structures, and optical properties of the cubic double perovskites Ba_2MgWO_6 and Ba_2ZnWO_6

Daniel E. Bugaris, Jason P. Hodges, Ashfia Huq and Hans-Conrad zur Loye

page 2293

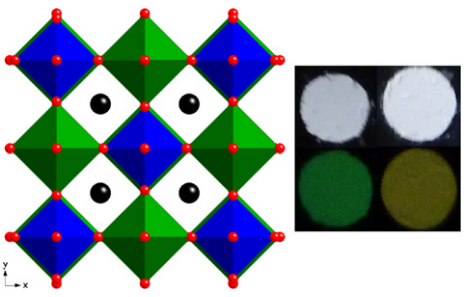

Ba_2MgWO_6 and Ba_2ZnWO_6 adopt the cubic double perovskite structure. Both compounds luminesce under UV irradiation, with green and yellow emissions, respectively.

Preparation and formation mechanism of three-dimensionally ordered macroporous (3DOM) MgO, $MgSO_4$, $CaCO_3$, and $SrCO_3$, and photonic stop band properties of 3DOM $CaCO_3$
Masahiro Sadakane, Rika Kato, Toru Murayama and Wataru Ueda
page 2299

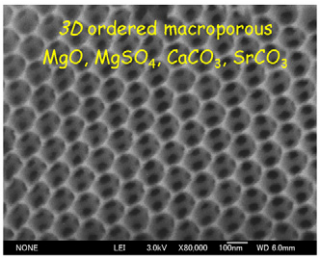

Well-ordered 3-dimensionally ordered macroporous MgO, $MgSO_4$, $CaCO_3$, and $SrCO_3$ materials were obtained in a high pore fraction.

Synthesis and oxygen content dependent properties of hexagonal $DyMnO_{3+\delta}$
S. Remsen, B. Dabrowski, O. Chmaissem, J. Mais and A. Szewczyk
page 2306

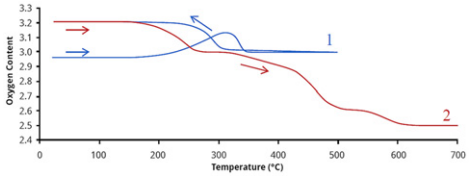

Thermogravimetric annealing in 21% O_2 after initial synthesis of $DyMnO_{3+\delta}$ in argon (curve 1) and subsequent reduction in 42% H_2 to Dy_2O_3 and MnO (curve 2).